Integrating reconstructed scatterometer and advanced very high resolution radiometer data for tropical forest inventory

Perry J. Hardin
Brigham Young University
Department of Geography
690 H SWKT
P.O. Box 25468
Provo, Utah 84602-5468
E-mail: perry_hardin@byu.edu

David G. Long
Brigham Young University
Department of Electrical and Computer Engineering
459 Clyde Building
P.O. Box 24099
Provo, Utah 84602-4099

Abstract. A scientific effort is currently underway to assess tropical forest degradation and its potential impact on Earth's climate. Because of the large continental regions involved, Advanced Very High Resolution Radiometer (AVHRR) imagery and its derivative vegetation index products with resolutions between 1 and 12 km are typically used to inventory the Earth's equatorial vegetation. Archival AVHRR imagery is also used to obtain a temporal baseline of historical forest extent. Recently however, 50-km Seasat-A Scatterometer (SASS) Ku-band imagery (acquired in 1978) has been reconstructed to ≈ 4-km resolution, making it a supplement to AVHRR imagery for historical vegetation assessment. In order to test the utility of reconstructed Ku-band scatterometer imagery for this purpose, seasonal AVHRR vegetation-index and SASS images of identical resolutions were constructed. Using the imagery, discrimination experiments involving 18 vegetation categories were conducted for a central South America study area. The results of these experiments indicate that AVHRR vegetation-index images are slightly superior to reconstructed SASS images for differentiating between equatorial vegetation classes when used alone. However, combining the scatterometer imagery with the vegetation-index images provides discrimination superior to any other combination of the data sets. Using the two data sets together, 90.3% of the test data could be correctly classified into broad classes of equatorial forest, degraded woodland/forest, woodland/savanna, and *caatinga*.

Subject terms: optical remote sensing; image processing; Seasat-A scatterometer; advanced very high resolution radiometer; NDVI; enhanced resolution image reconstruction.

Optical Engineering 34(11), 3146–3153 (November 1995).

1 Introduction

Currently there is an extended international effort to inventory and monitor the earth's global rain forests.[1] Because of persistent cloud cover in the equatorial regions where these forests are found, active microwave sensors, which can penetrate clouds, are preferable to visible and near-infrared spaceborne sensors. Nevertheless, Advanced Very High Resolution Radiometer (AVHRR) imagery and its derivative vegetation indices are frequently utilized for inexpensive medium- or low-resolution monitoring where comprehensive high-resolution imaging with Landsat-class satellites would be cost-prohibitive.

AVHRR imagery is also available for historical inventory. Data collected as early as 1978 are available from National Oceanic and Atmospheric Administration (NOAA) Tiros-N archives. The popular NOAA vegetation-index product, using data from NOAA-7 and other follow-on missions, is an extensive data set covering the period from May 1982 to the present. It is currently used for a variety of research tasks related to global change and climate.

Despite its availability and low cost, the utility of AVHRR's passive-sensor data is limited by the heavy convective cloud cover typical of equatorial regions. Clearly an active microwave instrument with 1- to 16-km resolution would be a desirable alternative data source to AVHRR under these conditions, but no active microwave device designed to provide global land coverage at this resolution has ever flown, and none are currently planned for the future.

Although their native spatial resolution is coarse (≈25 to 50 km), satellite scatterometers may nonetheless become an inexpensive alternative to AVHRR for equatorial forest monitoring. Satellite scatterometers are active microwave radar instruments designed to measure the radar backscatter of the ocean's surface under all-weather conditions. Between June and October of 1978, the Seasat-A Satellite Scatterometer (SASS) was able to obtain nearly global coverage at a spatial

Paper RS-008 received Apr. 3, 1995; revised manuscript received June 1, 1995; accepted for publication June 19, 1995.

unit-cell resolution of 50 km until a catastrophic hardware failure terminated data acquisition. The primary mission for SASS was to determine the ocean surface wind direction and velocity, not to acquire imagery for continental applications. This is not surprising, because most land imaging problems require minimum spatial resolutions approaching AVHRR global area coverage (4 km). In 1993, Long et al. introduced a method for reconstructing SASS imagery to 5-km resolution.[2] It was determined that this enhanced-resolution scatterometer data could be used for discriminating between broad equatorial vegetation types.[3] Given the success of these experiments, Long and Hardin proposed that future scatterometers be modified to perform a dual role as active microwave instruments equivalent to AVHRR in global coverage and spatial resolution. The use of reconstructed SASS imagery for historical rain-forest mapping was also suggested as a possible application of the technology.[4]

While these early successes with reconstructed scatterometry are encouraging, no one has empirically compared reconstructed SASS imagery with traditional AVHRR imagery for classifying equatorial vegetation into mappable classes. This is the motivation for the research reported here. This paper summarizes our experiments to compare AVHRR vegetation-index products with reconstructed SASS imagery for discriminating between 18 tropical vegetation classes. Analyzing seasonal SASS and AVHRR data sets, we determined that tropical vegetation discrimination with AVHRR vegetation-index images was slightly superior to classification using reconstructed SASS imagery. However, this was true only when the AVHRR and SASS data sets were employed separately. We also found that the accuracy produced by integrating the AVHRR and SASS data was distinctly superior to accuracies available by using only AVHRR imagery. In conclusion, we suggest combining historical AVHRR data with reconstructed SASS data for establishing a historical rain-forest baseline. Noting the planned launch of the NASA scatterometer (NSCAT) in 1996,[5] we suggest that reconstructed NSCAT imagery, when combined with future AVHRR data, will provide an important integrated data set for the study of global change.

2 SASS Image Reconstruction

Spaceborne scatterometers transmit microwave pulses to the ocean surface and measure backscattered power received at the instrument, allowing estimation of the normalized radar cross section (σ°) of the surface. From each illuminated location on the earth, the total power received by a radar is the sum of the power backscattered by the target, noise from the frequency-specific natural emissivity of the earth-atmosphere system, and noise from the instrument itself. Once the noise is subtracted from the total received power, σ° can then be calculated using the basic radar equation.[6]

SASS was designed to make nominally 50-km-resolution measurements of the normalized Ku-band radar backscatter coefficient at two azimuth angles over two 500-km-wide swaths separated by a 400-km nadir gap. From measurements of σ° over the ocean, the near-surface wind vector was inferred using a geophysical model function relating σ° and the wind vector.[5]

Although it was primarily designed for oceanic wind studies, data from SASS were also collected over global regions of ice and land during the flight of Seasat-A between June 27 and October 10, 1978. Although the intrinsic resolution of SASS was approximately 50 km, Long et al. developed a method to algebraically reconstruct medium-scale imagery with pixel resolutions between 4 and 12 km over land from these lower-resolution scatterometer measurements acquired at a variety of incidence and azimuth angles.[2] Assuming no azimuthal modulation over the narrow incidence-angle range between 23 and 55 deg, the incidence-angle dependence of σ° used by Long et al. can be described by

$$10 \log_{10}\sigma^\circ(\theta) = A + B(\theta - 40 \text{ deg}) , \quad (1)$$

where A and B are independent of the observation incidence angle θ and dependent only on the observed surface characteristic.[2,7] In this model, A is the value of σ° at an incidence angle of 40 deg; A can thus be considered the "incidence-angle-normalized" σ°. Because of the diversity of incidence angles used in acquiring SASS measurements, the coefficients A and B of this model are more useful in application than the direct σ° measurements.[2,3] In practical terms, although images of A and B are produced in the reconstruction process, only the A image has been used for traditional image classification.[4]

The key to achieving high resolution by signal processing is the spatial overlap in the original SASS σ° measurements. However, the SASS σ° measurements made during a single orbit did not have sufficient overlap to attempt the resolution enhancement scheme. Due to precession in the spacecraft orbit, a point on the earth's surface was observed by the same beam with slightly different azimuth and incidence angles about once every three days. Data were also acquired by the instrument on both ascending and descending orbital nodes. The resulting set of criss-crossing measurement swaths over several days provides ample overlap to facilitate accurate estimation of A over equatorial regions. It must be kept in mind that the reconstructed A image represents the entire data-acquisition time span (days to months) rather than a single time "snapshot." In broad terms, A constitutes a weighted temporal average of the original σ° measurements.[2]

The ultimate resolution obtainable with the reconstruction technique depends on the original measurement-cell overlap and the measurement noise. Arbitrarily reducing the size of resolution elements does not increase the effective resolution of the resulting A image, since the noise in the image *increases* as the resolution-element size is *decreased.* To minimize the estimate noise for a given resolution-element size, the number of measurement cells should be maximized. This however increases the imaging time interval necessary to gather the measurements. Depending on the season and region, using long imaging intervals is questionable, since the target may change over time. In practice, selecting the enhanced resolution element size involves a trade-off between the required imaging time interval and the acceptable image estimate noise level.

Hardin and Long have discussed the criteria that a target must satisfy to obtain an enhanced-resolution reconstructed A image suitable for land-cover analysis.[4] These may be summarized as follows:

1. The dependence of σ° on time of day, azimuth angle, and topography is negligable.

2. The coefficients A and B remain constant for the data acquisition period.
3. Over the range of incidence angles used for the reconstruction, the linear model describes the incidence-angle dependence of σ° for the target.
4. Heavy continuous rainfall does not persist for the data acquisition period.

Hardin and Long discuss at length how these criteria are satisfied in the South America study area.[4] However, since cloud cover and its associated heavy rainfall have always been a potential problem in utilizing AVHRR over equatorial regions, the last criterion deserves elaboration.

It is common knowledge that rainfall can attentuate backscatter at Ku-band frequencies. In a preliminary analysis of Amazon region SASS data, Birrer et al. corrected for this attenuation by using geostationary satellite imagery to remove all SASS measurements that showed significant cloud cover. The procedure was deemed unnecessary and abandoned, because "few measurements should have been corrupted" by the dry-season acquisition.[7]

3 AVHRR and the Global Vegetation Index Products

The AVHRR instruments that flew on polar orbiters NOAA-7, NOAA-9, and NOAA-11 were five-channel radiometers capable of continuously scanning the earth with 1-km ground resolution. While these 1-km data are available for limited portions of the Earth, AVHRR global area coverage (GAC) data are resampled on board the satellite to 4-km resolution and stored for later transmission to Earth receiving stations. The five channels used by the instrument cover the following spectral ranges:

1. 0.58 to 0.68 μm
2. 0.725 to 1.10 μm
3. 3.55 to 3.93 μm
4. 10.30 to 12.50 μm
5. 11.50 to 12.50 μm.

Early work by Tarpley et al. and others demonstrates that vegetation indices derived from NOAA polar orbiter sensors such as AVHRR are extremely useful for monitoring vegetation on a continental scale.[8] Several vegetation indices used with AVHRR are reported in the literature. One of the simplest, designated in this research as IR/R, is defined as

$$\text{IR/R} = \text{Channel 2/Channel 1} .$$

In contrast, the normalized difference vegetation index (NDVI), derived from AVHRR channels, is defined as

$$\text{NDVI} = \text{Channel 2} - \text{Channel 1/Channel 2} + \text{Channel 1} .$$

For most applications, NDVI is preferred to IR/R because it helps mitigate the effects of viewing aspect, terrain slope, and changes in illumination.[9]

The AVHRR global vegetation index (GVI) product, produced by NOAA, is an extensive collection of daily, weekly, and biweekly vegetation-index images available in a variety of map projections. These images are composites derived from daily AVHRR GAC data. Like reconstructed SASS data, GVI imagery is a composite of several original images acquired over time. As described by Ohring et al., an individual pixel on the weekly image composite is produced by scanning the corresponding pixel on the daily images for "greenest" or most "cloud-free" value. The greenest pixel for any week is the pixel having the greatest channel 2–channel 1 difference. Once this pixel value is determined, it is then assigned to that pixel location in the weekly image composite. When performed for all the image pixels, it is thought that this assignment method significantly lowers the effect of cloud cover.[10] In order to offer users maximum flexibility, the GVI product created before April 1985 consisted of AVHRR channel 2, channel 1, NDVI, and the channel 2–channel 1 difference images.

A processing overview of the first- and second-generation GVI products is described by Kidwell.[9] NOAA is now completing its third-generation products. The first-generation products used in this study were experimental, and have a few inherent limitations. First, the imagery is cast in two hemispheric polar stereographic projections with the resolution changing from 13 km at the equator to 26 km at the poles. This projection is inconvenient for equatorial studies, since the area of interest is split between the two hemispheres in the projection. This is a nuisance to visualization, interpretation, and registration. Secondly, the processing methodology to combine the daily data into weekly data changed three times over the study period used in 1982. The reader is invited to review Kidwell's discussion of these processing changes.[9] In this research, these processing differences are effectively noise. Other limitations in the GVI products, along with suggestions for their correction, are summarized in Tatesishi and Kajiwara[11] and Kaufman et al.[12]

4 Comparison Methodology

4.1 *The SASS Imagery*

The reconstructed SASS A image used in the comparison was composited from data collected over central South America from July 1 to October 10, 1978. While SASS was capable of making both vertically and horizontally polarized measurements of the radar backscatter, only vertically polarized data were used in this study. Additionally, orbits for which the spacecraft attitude determination was in error were excluded.[13] Only σ° values in the incidence-angle range from 23 to 55 deg with noise below a certain predetermined level were used as data for the reconstruction. The final SASS A image was cast on a latitude-longitude projection with a grid cell resolution of approximately 5 km. The image is shown in Fig. 1.

4.2 *The GVI Imagery*

As mentioned above, the SASS A image is a seasonal composite using data acquired between July 1 and October 10, 1978. In order to fairly compare the SASS A and GVI products, GVI composites were constructed for the same seasonal period, albeit in 1982. This was the earliest GVI imagery available. Nineteen GVI image data sets corresponding to the weeks between Monday, May 31, and Sunday, October 10, 1982, were averaged on a pixel-by-pixel basis to produce the required seasonal GVI composites—one composite rep-

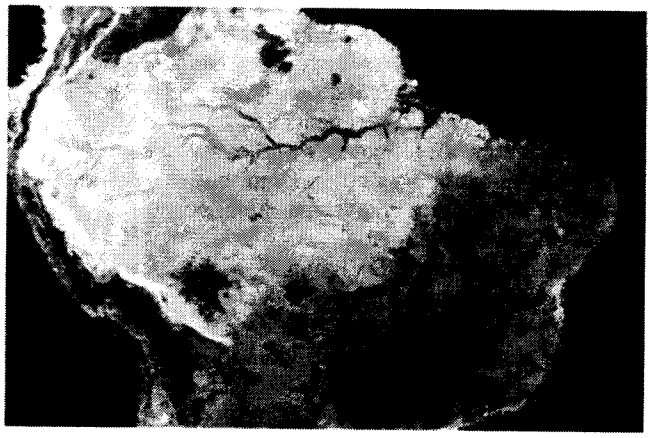

Fig. 1 The reconstructed SASS *A* image of the South America study area.

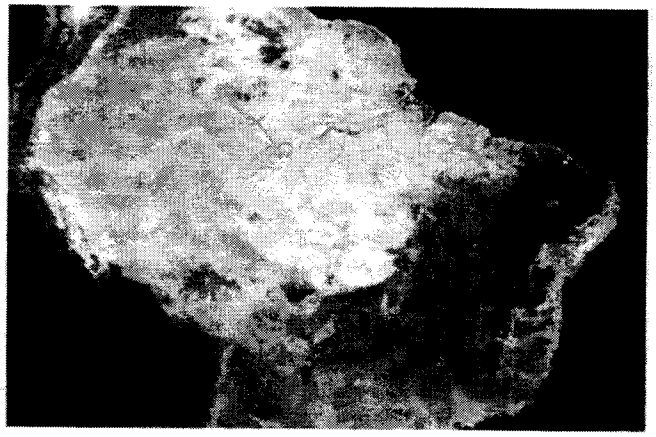

Fig. 2 The seasonal NDVI image of the South America study area.

resenting seasonal NDVI, and the other representing the seasonal IR/R ratio. These composites, originally cast on a polar stereographic projection, were recast to the same latitude-longitude graticule as the SASS image to achieve precise registration of the three data sets. This was performed by in-house computer routines that interconvert satellite imagery between polar stereographic and latitude-longitude projections using exact forward and inverse projection formulas. No operator intervention was required. Since the pixel size of the GVI data set in this region (approximately 14 km) was much coarser than the SASS data set, nearest-neighbor interpolation was utilized to fill the 5-km pixels in the final GVI images. The NDVI image is shown in Fig. 2. The IR/R image is similar in appearance. Relationships between features in Figs. 1 and 2 are obvious.

4.3 *Classification Process*

The goal of the classification process was to determine whether SASS *A* imagery was superior to NDVI and IR/R for discriminating between tropical vegetation classes within the study area (see Fig. 3). Using the 1 : 5,000,000-scale *Vegetation Map of South America,*[14] several polygons were delimited for 18 equatorial and subtropical vegetation formations. Realizing the limitations of the map source material, the inexact nature of cartographic classification, unavoidable generalizations, and the difficulties in drawing exact boundaries for vegetation classes that likely blend in transition zones, the polygons were delimited only for the larger mapped areas of vegetation. Once these polygons were digitized, the corresponding pixels were extracted from the SASS *A*, IR/R, and NDVI images and saved for further analysis.

The analysis consisted of two parts. In the first part, the objective was to explore the relationship between the vegetation index and *A* values for each vegetation formation. Since the backscatter response of tropical vegetation at Ku-band frequencies and continental scales is badly known, it was hoped that this examination would provide insight into scattering mechanisms.

In the second part, exploratory discrimination analysis was performed to determine which combination of the three data sets (*A*, NDVI, IR/R) would be superior for classifying the vegetation formations. Since seven combinations were possible, seven discrimination experiments were conducted:

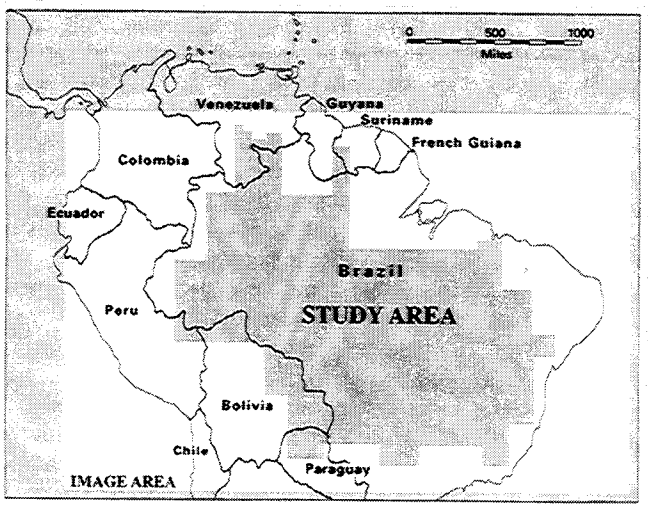

Fig. 3 The study area.

1. Discrimination using IR/R alone
2. Discrimination using NDVI alone
3. Discrimination using *A* alone
4. Discrimination using IR/R and NDVI together
5. Discrimination using *A* and IR/R together
6. Discrimination using *A* and NDVI together
7. Discrimination using *A*, IR/R, and NDVI together.

In the discrimination test results reported below, only one-half of the pixels for each of the 18 formations were used for training the classifier, while the remaining half were reserved for testing the accuracy of the discrimination. The formula used for determining the discriminant-function distance between test pixel x and vegetation group h was

$$F_{xh} = \mathbf{C}_h^T \mathbf{x} + \Theta_h + \ln p_h \ ,$$

where

$$\mathbf{C}_h^T = \boldsymbol{\mu}_h^T \mathbf{S}^{-1} \quad \text{and} \quad \Theta_h = -\frac{1}{2} (\boldsymbol{\mu}_h^T \mathbf{S}^{-1} \boldsymbol{\mu}_h) \ .$$

The reader will recognize this as Fisher's linear discriminant function. Using the seventh discrimination experiment enumerated above as an example, $\boldsymbol{\mu}_h$ is the vector of means on *A*, NDVI, and IR/R for vegetation group *h*. The matrix $\mathbf{S}^{-1}$ is the inverse of the pooled covariance matrix for all the vegetation groups, and the vector $\mathbf{x}$ represents the values of *A*, NDVI, and IR/R for test pixel *x*. The variable p_h is the prior probability for class *h*. When employing this function, the distance F_{xh} was calculated between the unlabeled test pixel and each vegetation group. The pixel was then assigned the vegetation label of the group that generated the smallest F_{xh} value. In order to remain conservative in our methodology, the prior probabilities for each vegetation class (p_n) were assumed equal.

The fundamental approach used in the exploratory discriminant analysis was to continually regroup the original 18 categories into a much smaller set until the classification accuracy produced by the discriminant functions reached an acceptable level. An effort was made to maintain logically consistent groupings. For example, while woodland categories could be combined with forest categories, forest and grassland categories were not joined.

In simple terms, the quality of the discriminations was assessed by counting the number of test pixels placed in the correct vegetation class by the discriminant function. A simple percentage of agreement was then calculated. Cohen's kappa (κ) was calculated for each classification. The statistic κ is a metric that, unlike a simple percentage, allows for the classification accuracy that could be expected by the operation of chance alone. (The reader unfamiliar with κ may wish to review Congalton, Oderwald, and Mead[15] for a discussion of its calculation and merits.) In comparing classifications, κ is a more conservative, useful measure of discriminating power than the simple percentage, particularly in experiments producing low classification accuracies and/or involving very few classes. A κ of 0.0 indicates that there is no discrimination between the classes, while a κ of 1.0 indicates that errorless discrimination was achieved. The variance for κ can also be calculated, allowing different classifications to be assessed for statistically significant differences.[15] These calculations were performed for the seven discrimination experiments and tabulated.

In interpreting the κ figures, we note that the sample drawn for the classification was not random, but was delimited by drawing a polygon around various homogeneous vegetation regions. Furthermore, spatial autocorrelation, which is likely to exist within the *A*, NDVI, and IR/R data, technically violates the assumption of independence of observations required for valid significance tests. In order to see how sensitive our results were to these violations, we stratified the entire data set by polygon, and extracted 5000 random pixels. The discrimination analyses were then conducted again. This process was repeated three times, using a different sample for each repetition. The results produced from the samples did not differ substantially from results using the entire data set of 38,534 pixels. In some cases the accuracy values were slightly lower or higher (almost always less than 1 percentage point), but never did the values contradict the results using the entire data set.

5 Results

A statistical summary of the 18 vegetation classes is given in Table 1. The table, sorted by *A* value, includes both the training and the test pixels. In general, the forest types had the highest *A* values, followed by the degraded forest, woodland classes, *caatinga*, and grassland classes. The NDVI class mean values showed the same general trend for larger to smaller values. As illustrated in Figs. 4 and 5, the correlation between the two indexes and the SASS *A* data is moderate ($r_{IR/R,A}=0.799$, $r_{NDVI,A}=0.763$, $p<0.05$). It seems that the biophysical parameters affecting the vegetation-index values are reflected in the *A* data. The *caatinga* classes are notable exceptions to the general linear relationship between the *A* and vegetation-index values. The low *caatinga* NDVI (<0.1) can be attributed to the general character of a xerophytic woodland in the dry season, where actual leaf area is ex-

Table 1 Descriptive statistics for the 18 vegetation classes in the study area. Horizontal lines delimit classes combined in the four-group discrimination experiment; *n* = number of pixels; *s* = standard deviation.

Class Name	*n*	*A*	s_A	NDVI	s_{NDVI}	IR/R	$s_{IR/R}$
Extremely moist forest (Em)	476	-7.205	0.190	0.283	0.033	1.794	0.122
Ombrophilous submontane forest (Os)	585	-7.472	0.944	0.289	0.034	1.820	0.131
Moist seasonal forest (Sm)	4200	-7.545	0.205	0.286	0.015	1.802	0.059
Very moist forest (Vm)	9601	-7.668	0.230	0.292	0.018	1.828	0.070
Tropical seasonal lowland forest (Tsl)	600	-7.843	0.611	0.280	0.034	1.784	0.127
Degraded forest formation (Df)	243	-7.551	0.392	0.258	0.022	1.698	0.078
Degraded deciduous woodland (Ddw)	999	-8.592	0.366	0.252	0.023	1.676	0.081
Caatinga (Ca)	1866	-9.329	0.674	0.075	0.037	1.167	0.093
Degraded *caatinga* formation (Dca)	336	-9.805	0.449	0.094	0.022	1.209	0.055
Chaco (Ch)	5184	-9.452	0.484	0.162	0.032	1.389	0.090
Campos cerrados north (Ccn)	3922	-10.055	0.696	0.151	0.022	1.357	0.062
Campos sujos / limpos (Csl)	2030	-10.140	1.653	0.192	0.067	1.493	0.215
Pantanal (Pa)	2116	-10.322	0.945	0.178	0.026	1.436	0.078
Cultivated crops (Cr)	2545	-10.461	0.893	0.165	0.022	1.398	0.061
Degraded lowland woodlands (Dlw)	668	-10.675	0.564	0.152	0.025	1.360	0.068
Grassland with palms (Gp)	643	-10.748	1.149	0.210	0.037	1.536	0.119
Campos cerrados south (Ccs)	1836	-10.936	0.731	0.175	0.019	1.427	0.055
Degraded *campos cerrados* (Dcc)	684	-11.180	0.508	0.144	0.017	1.338	0.046

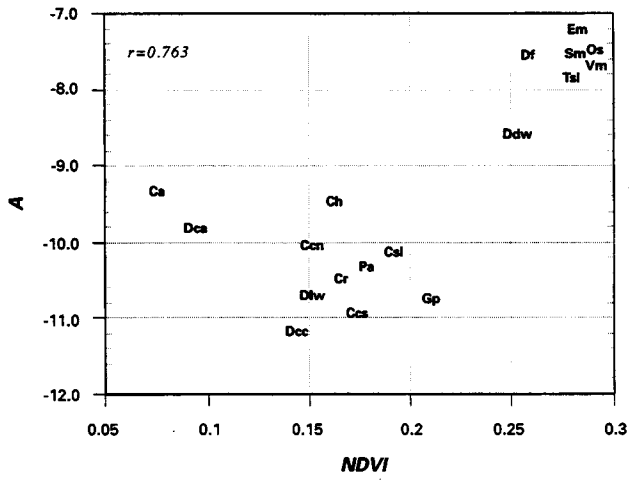

Fig. 4 NDVI versus SASS *A* graph of class means for the 18 vegetation categories. The abbreviations are listed in Table 1. Note how the *caatinga* classes deviate significantly from the general linear relationship.

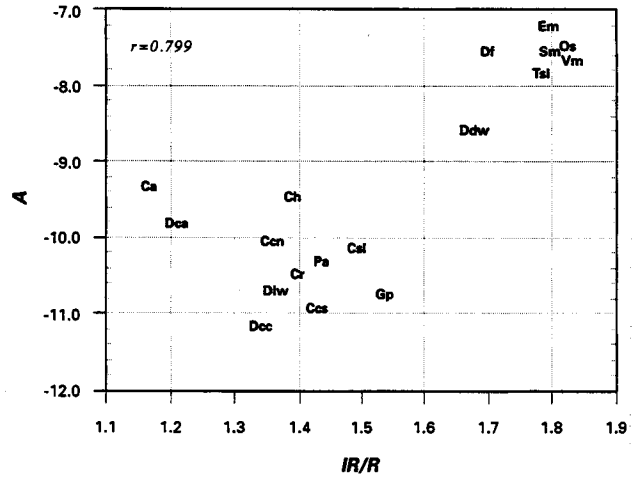

Fig. 5 IR/R versus SASS *A* graph of class means for the 18 vegetation categories. The abbreviations are listed in Table 1. Note how the *caatinga* classes deviate significantly from the general linear relationship depicted.

tremely limited; but we cannot explain the *caatinga* midrange values of *A*. We suspect that the bare soil typical of *caatinga* is a strong contributing factor.

The results of the 18 group discrimination experiments are shown in Table 2. Using the *A* data alone, only 18.4% of the vegetation pixels were properly classified. The AVHRR vegetation indices performed only slightly better, with NDVI and IR/R producing percentages of 24.8 and 26.7 respectively. The best results were obtained by combining the *A* data with one of the AVHRR indices. As shown in Table 2, there was no significant difference in classification accuracy when IR/R was substituted for NDVI in combination with the *A* data.

After attempting to discriminate between all 18 formations, the vegetation categories were combined and the classification experiments repeated. Table 3 shows the confusion matrix resulting from the final four group classification utilizing both *A* and NDVI as discriminating variables. As shown there, the final groups can be broadly labeled as forest, degraded woodland/forest, woodland/savanna, and *caatinga*. Misclassification between the groups is plausibly distributed. For example, the forest group is confused somewhat with the degraded forest/woodland group, but there is little confusion between forest and *caatinga*. While we would expect degraded forest to be confused somewhat with untouched forest, we would not expect those same wet forests to be confused with xerophytic *caatinga*.

Table 2 Results of the 18 group classification experiment, sorted by κ. An asterisk (*) indicates a classification significantly ($p<0.05$) superior to the classification in the preceding row of the table.

Discrimination Variables	% correct	Kappa (κ)	Variance (s^2_κ)
A	18.4	0.136	7.30×10^{-7}
IR/R NDVI	22.7	0.175*	9.08×10^{-6}
NDVI	24.8	0.181	9.25×10^{-6}
IR/R	26.7	0.198*	1.00×10^{-5}
A, NDVI	39.1	0.331*	1.30×10^{-5}
A, IR/R	40.1	0.340	1.32×10^{-5}
A, IR/R, NDVI	39.7	0.344	1.31×10^{-5}

Results from the four-group discrimination experiments are summarized in Table 4. The pattern established in the 18-group experiment is apparent in this experiment as well. While the *A* data constituted the poorest discriminator when used alone, the highest accuracies were achieved by combining them with the vegetation indices. Specifically, the highest classification accuracy was achieved by combining *A* with the NDVI information (90.3%, $\kappa = 0.84$). Based on κ, this classification is significantly better than its closest competitor ($p<0.05$).

6 Conclusions

Given the success of these discrimination experiments, further research into combining SASS and AVHRR data may provide significant advances in monitoring equatorial regions from space. Monitoring global rain forests requires that changes from forest to degraded forest and other categories be accurately classified and mapped. In the future, much of the confusion in pure AVHRR optical-infrared classifications could be removed by integrating reconstructed scatterometer images using a methodology similar to the one described in this report. With the launch of ADEOS and the enhanced-resolution ground processing of NSCAT imagery, the probability of successfully integrating the two data sources is high. Unlike the SASS data, which covered only three months, NSCAT and AVHRR coverage of the equatorial and savanna regions for the entire year will allow the change in backscatter, NDVI, and IR/R to be monitored throughout an annual cycle and used as a discriminator for more accurate

Table 3 Confusion matrix produced in the four-group experiment using *A* and NDVI as discriminating variables. The overall classification accuracy is 90.3%.

	Predicted Group			
Actual group	Forest	Degraded woodland and forest	Caatinga	Woodland and savanna
Forest (Tsl, Em, Sm, Os, Vm)	7177	527	5	21
Degraded woodland and forest (Ddw, Df)	112	475	1	32
Caatinga (Ca, Dca)	0	14	1000	87
Woodland and savanna (Dcc, Ccn, Ch, Cr, Ccs, Pa, Csl, Gp, Dlw)	160	504	416	8733

Table 4 Results from the four-group discrimination experiments, sorted by κ. An asterisk (*) indicates a classification is significantly ($p<0.05$) superior to the classification in the preceding row of the table.

Discrimination Variables	% correct	Kappa (κ)	Variance (s^2_κ)
A	72.5	0.436	1.78×10^{-5}
IR/R	84.6	0.699*	2.13×10^{-5}
IR/R NDVI	85.1	0.761*	1.47×10^{-5}
NDVI	85.6	0.767	1.46×10^{-5}
A, IR/R, NDVI	87.5	0.796*	1.34×10^{-5}
A, IR/R	88.7	0.814*	1.27×10^{-5}
A, NDVI	90.3	0.838*	1.15×10^{-5}

vegetation mapping. A yearly comparison of the two image types would also help in understanding the mechanisms of backscatter at Ku-band frequencies at moderate resolutions. It may also be possible to utilize reconstructed NSCAT imagery (which is less prone to cloud-cover problems) to better calibrate AVHRR imagery and the GVI products.

While the future of integrating reconstructed scatterometry imagery with AVHRR is untested, the use of reconstructed SASS data as a historical data source is more obvious. Given adequate effort, it will be reasonable to extend the SASS reconstruction procedure for the subtropical globe so it can be integrated with AVHRR data sets of similar age. The results of this study indicate that a highly accurate baseline of forest extent would be possible with the combined data sets.

The potential for utilizing the SASS-AVHRR image set may go beyond land-cover mapping and monitoring. The existence of several vegetation-class gradations within and between the vegetation formations, along with the moderate correlation between the backscatter and vegetation-index values, indicates the possibility of obtaining critical quantitative information about subtropical vegetation community character from these integrated sources. While the correlation between the *A* and GVI images leads us to believe that 14.6-GHz backscatter in equatorial areas is a function of canopy density or leaf area, it is possible these backscatter coefficients also change in response to canopy vigor, canopy moisture, other canopy structural characteristics, or more complex quantitative variables. The existence of the *caatinga* outliers indicates that the information in the SASS *A* was not redundant. Another physical mechanism besides leaf area was operating to produce the outliers. Using higher-resolution SAR, visible, thermal, and infrared imagery of carefully selected field sites as primary data sources, it may be possible to use enhanced-resolution reconstructed scatterometer imagery and AVHRR imagery together in order to extend derived estimates of biomass, canopy structure, moisture content, or transpiration rates over large regions.

7 Definitions

The definitions below were adapted from UNESCO.[16]

- *Caatinga*: Semideciduous thorn scrub with succulents. Climax *caatinga* is ligneous, drought-deciduous, thickly branched, narrow-leaved, and sometimes thorned. In some areas it may resemble steppe, and in other regions it may be a dense scrubland with canopies reaching 10 m. Cactus may also be found.
- *Chaco*: Drought deciduous lowland and submontane woodland. This woodland is typically multicanopied, with cactus in drier areas. There are many climatic and edaphic variations on a local scale.
- *Campo cerrado*: Medium-tall grassland with several species of broad-leaved evergreen trees and shrubs. In general, southern *campo cerrado* is distinguished from northern communities by its shorter dry season, definite cool season, and denser understory.
- *Campos sujo/limpo*: Prairie grassland nearly devoid of shrubs (*limpo*) or having scattered shrubs (*sujo*).
- *Pantanal*: Primarily a humid savanna of hygrophytic grassland, 80% flooded during the rainy season. In areas of higher local relative relief, this grassland is replaced by shrubs, woodland, and forest.

Acknowledgments

We wish to acknowledge the support of R. Thomas at NASA Headquarters. SASS data were obtained from the NASA Physical Oceanography Distributed Active Archive Center at the Jet Propulsion Laboratory, California Institute of Technology. We also wish to thank Intergraph Corporation (manufacturer of MGE geographic information system and image processing software) for its continued support of theoretical and applied environmental remote sensing.

References

1. "Strategy Proposal 1991–1992," Trees Technical Ser. A, No. 1, A Joint Project of the Commission of the European Communities and the European Space Agency, SPI.90.31, Joint Research Center, Ispara, Italy (1991).
2. D. G. Long, P. J. Hardin, and P. T. Whiting, "Resolution enhancement of spaceborne scatterometer data," *IEEE Trans. Geosci. and Remote Sensing* **31**(3), 700–715 (1993).
3. D. G. Long and P. J. Hardin, "Vegetation studies of the Amazon basin using enhanced resolution Seasat scatterometer data," *IEEE Trans. Geosci. and Remote Sensing* **32**(2), 449–460 (1994).
4. P. J. Hardin and D. G. Long, "Discriminating between tropical vegetation formations using reconstructed high-resolution Seasat-A scatterometer data," *Photo. Eng. and Remote Sensing* **60**(12), 1453–1462 (1994).
5. F. M. Naderi, M. H. Freilich, and D. G. Long, "Spaceborne radar measurement of wind velocity over the ocean: An overview of the NSCAT scatterometer system," *Proc. IEEE* **79**(6), 850–866 (1992).
6. F. T. Ulaby, R. K. Moore, and A. K. Fung, *Microwave Remote Sensing—Active and Passive*, Vols. 1, 2, Addison-Wesley, Reading, MA (1981).
7. I. J. Birrer, E. M. Bracelente, G. J. Dome, J. Sweet, and G. Berthold, "σ° signature of the Amazon rainforest obtained from the Seasat scatterometer," *IEEE Trans. Geosci. and Remote Sensing* **GE-20**, 11–17 (1982).
8. J. D. Tarpley, S. R. Schneider, and R. L. Money, "Global vegetation indices from NOAA-7 meteorological satellite," *J. Climatol. and Appl. Meteorol.* **23**, 491–494 (1984).
9. K. B. Kidwell, *NOAA Polar Orbiter Data User's Guide*, NOAA/NESDIS, Washington (1986).
10. G. Ohring, K. Gallo, A. Gruber, W. Planet, L. Stowe, and J. D. Tarpley, "Climate and global change: characteristics of NOAA satellite data," *EOS, Trans. Amer. Geophys. Union* **70**(41), 889–901 (1989).
11. R. Tateishi and K. Kajiwara, "Global land cover monitoring by NOAA GVI data," in *IGARSS '92*, Vol. 2, pp. 1637–1639, IEEE, New York (1992).
12. Y. J. Kaufman, D. Tanré, B. N. Holben, B. Markham, and A. Gitelson, "Atmospheric effects on the NDVI—strategies for its removal," in *IGARSS '92*, Vol. 2, pp. 1238–1241, IEEE, New York (1992).
13. E. M. Bracelente and J. L. Sweet, "Analysis of normalized radar cross section (σ°) signature of Amazon rain forest using Seasat scatterometer data," NASA Technical Memorandum 85779, NASA NTIS (1984).
14. UNESCO, *Vegetation Map of South America. 1 : 5,000,000*, two sheets, United Nations Educational, Scientific, and Cultural Organization, Paris (1980).
15. R. G. Congalton, R. G. Oderwald, and R. A. Mead, "Assessing Landsat classification accuracy using discrete multivariate analysis statistical techniques," *Photo. Eng. and Remote Sensing* **49**(12), 1671–1678 (1983).
16. UNESCO, *Vegetation Map of South America Explanatory Notes*, United Nations Educational, Scientific, and Cultural Organization, Paris (1981).

Perry J. Hardin is an associate professor in the Geography Department at Brigham Young University and directs the BYU Laboratory for Geographic Information Analysis. Holding a PhD in geography (remote sensing) from the University of Utah, he is an investigator on several projects involving the integration of remote sensing and GIS for resource management. His research interests include biogeography, image processing theory, climatology, and habitat modeling.

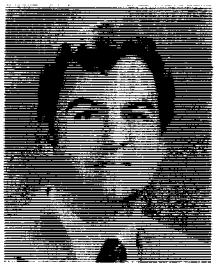

David G. Long is an associate professor in the Electrical and Computer Engineering Department at Brigham Young University and directs the BYU Microwave Remote Sensing Research Group. He has a PhD in electrical engineering from the University of Southern California. He is the principal investigator on several NASA-sponsored interdisciplinary research projects in remote sensing and has numerous publications in signal processing and radar scatterometry. His research interests include microwave remote sensing, radar, signal processing, and mesoscale atmospheric dynamics.